Application of POSS Nanotechnology for Preparation of Efficient Ni Catalysts for Hydrogen Production

I.Z. Ismagilov[1], E.V. Matus[1], V.V. Kuznetsov[1], S.A. Yashnik[1], M.A. Kerzhentsev[1], G. Gerritsen[2], H.C.L. Abbenhuis[2], Z.R. Ismagilov[1,3]*

[1]Boreskov Institute of Catalysis SB RAS, pr. Akademika Lavrentieva, 5, 630090, Novosibirsk, Russia
[2]Hybrid Catalysis B.V., Den Dolech 2, Eindhoven 5612, AZ, the Netherlands
[3]Institute of Coal Chemistry and Material Science SB RAS, pr. Sovetskiy, 18, 650000, Kemerovo, Russia

Article info

Received:
14 August 2016

Received in revised form:
2 October 2016

Accepted:
28 November 2016

Keywords:
POSS nanotechnology;
nanomaterials;
Ni nanoparticles;
autothermal reforming
of methane;
hydrogen production.

Abstract

POSS (polyhedral oligomeric silsesquioxanes) nanotechnology was applied for preparation of efficient Ni catalysts for hydrogen production through autothermal reforming of methane (ATR of CH_4). The novel metal-POSS precursor [Nickel (II) – HeptaisobutylPOSS $(C_4H_9)_7Si_7O_9(OH)O_2Ni$] of Ni nanoparticles was introduced into $Ce_{0.5}Zr_{0.5}O_2$ support with following calcination and reduction stages of activation. The peculiarity of the genesis of $Ni/SiO_2/Ce_{0.5}Zr_{0.5}O_2$ nanomaterials and their characteristics versus deposition mode were studied by X-ray fluorescence spectroscopy, thermal analysis, N_2 adsorption, X-ray diffraction, high-resolution transmission electron microscopy and H_2 temperature-programmed reduction. The two kinds of supported Ni-containing particles were observed: highly dispersed Ni forms (1–2 nm) and large Ni-containing particles (up to 50–100 nm in size). It was demonstrated that the textural, structural, red-ox and, consequently, catalytic properties of ex-Ni-POSS catalysts depend on the deposition mode. The increase of a portion of difficultly reduced Ni^{2+} species is found upon application of intermediate calcination during Ni-POSS deposition that has detrimental effect on the activity of catalyst in ATR of CH_4. The $Ni/SiO_2/Ce_{0.5}Zr_{0.5}O_2$ catalyst prepared by one-step Ni-POSS deposition exhibits the highest H_2 yield – 80% at T = 800 °C.

1. Introduction

Development of efficient and low cost hydrogen production technologies is an urgent task due to the increased demand of clean energy generation [1–15]. At present more than 50 million tons of hydrogen are produced annually worldwide and much of this hydrogen is used in the chemical and refinery industries [15]. In the future, it is expected that H_2 could be widely used for power generation and in transport by fueling gas turbines, fuel cells and combustion engines [1–11]. The H_2 consumption rate steadily growths in the world and the 30% increase of global H_2 production is predicted in the next 5 years [15]. There are different technologies of hydrogen production using nonrenewable (natural gas reforming, coal gasification) as well as renewable (biomass processes, biological production etc.) resources, nuclear energy (high-temperature water splitting) and electricity (electrolysis of water) [3–9]. Although the "green" or carbon-neutral path from current fossil-based to future hydrogen economy is preferable and provides sustainable development [1–4], to date H_2 is usually produced from fossil fuels without CO_2 capture and storage [16, 10, 13]. Natural gas remains main feedstock for hydrogen production [8, 13, 14, 16, 17]. The typical technologies for production of hydrogen from natural gas are steam methane reforming (SMR), partial oxidation (POX) and autothermal reforming (ATR). ATR of CH_4 is actually the combined process of POX and SMR in one reactor. The generated heat from POX is used for an endothermic SMR reaction, thus providing advantages of ATR technology for hydrogen production. Ni-based catalysts have been used and widely studied in methane reforming because of their high catalytic activity and low price [16–24]. But under long exposure

*Corresponding author. E-mail: zinfer1@mail.ru

to ATR reaction conditions Ni-based catalysts suffer from deactivation through the sintering of active component, the phase transformations and the formation of carbonaceous deposits [25–27]. The stabilization of small Ni nanoparticles in the support matrix is one of the approaches to overcome these obstacles. To achieve this effect, the modification of support [28, 29], the improving of preparation method [30], the selection of appropriate metal precursor [31–34] and the optimization of catalyst activation conditions [35–38] are widely employed. Introduction of structural promoter (such as B [23] or Sn [39]) also helps to increase the Ni particle dispersion. It is demonstrated that B-promoted 30 wt.%Ni/$MgAl_2O_4$ catalyst has average Ni particle size of 6.4 nm while un-promoted Ni catalyst – 10.3 nm. It improves the catalyst resistance toward carbon deposition.

Selection of appropriate support is an important stage at the elaboration of effective catalyst. It was shown that the average Ni particle size rose from 6.7 to 17.5 nm in the following order of supports: La_2O_3/Al_2O_3 < $La_2O_3/Ce_{0.5}Zr_{0.5}O_2/Al_2O_3$ < Al_2O_3 < $Ce_{0.5}Zr_{0.5}O_2/Al_2O_3$ < CeO_2/Al_2O_3 < ZrO_2/Al_2O_3 [29]. The fixing of small Ni nanoparticles over La-modified support provides more stable performance of 10 wt.%Ni/$La_2O_3/Ce_{0.5}Zr_{0.5}O_2/Al_2O_3$ catalyst in comparison with 10 wt.%Ni/$Ce_{0.5}Zr_{0.5}O_2/Al_2O_3$ catalyst in ATR of CH_4 [40]. The analogous positive effect of 5–10 wt.% Y_2O_3 additive on the stability of Ni/Al_2O_3 catalyst in ATR of CH_4 was observed [41]. It is noted that Y_2O_3 hinders Ni sintering. In addition to the effect of support composition on the crystal size, reducibility and electron structure of active Ni species, support can take part in the intermediate steps of CH_4 conversion. Particularly, the investigation of a series of 5 wt.%Ni/xCeO_2-(1-x) ZrO_2-Al_2O_3 catalysts (x = 0.2, 0.4, 0.6, 0.8) in SMR shows that the highest methane conversion rate as well as the lowest carbon deposition is realized on the catalyst with the highest Ce content (x = 0.8) [42]. Authors noted that better results attained with 5 wt.%Ni/0.8CeO_2-0.2ZrO_2-Al_2O_3 catalyst are related with a smaller size of Ni particles and also with higher C gasification due to H_2O adsorption on segregated CeO_2 particles.

Mode of preparation has a pronounced effect on the catalyst performance in ATR of CH_4 through regulation of the nature of Ni species, Ni particle size and Ni reducibility [40, 43]. So for tuning the properties of Ni nanoparticles the various methods were applied for synthesis of the supported Ni catalysts: the incipient wetness impregnation [44], co-precipitation [45], deposition-precipitation [46], combustion [47, 48], sol-gel [49], surfactant assisted and polyol [50] methods. The use of methods which provide the realization of a strong metal-support interaction has positive effect on the long-term stability of catalysts in hydrocarbon reforming processes [51, 52]. In particular, it was shown that homogeneous deposition precipitation (HDP) method as compared with pore volume impregnation (PVI) method provides 20 wt.%Ni/$MgAl_2O_4$ catalyst with smaller Ni particle size [23]. The average Ni particle size is equal to 4.5 and 8.1 nm for the ex-HDP and ex-PVI catalysts, respectively. In this case, the reaction rate of catalysts in SMR increases linearly with the Ni dispersion, while the content of carbonaceous deposits decreases. Similar conclusion was made at comparative study of Ni catalysts synthesized by the polyol and surfactant-assisted methods [50]. In dry reforming of methane the polyol catalysts displayed the highest activity and selectivity, which can be connected with improved Ni dispersion and presence of stronger metal-support interaction in these catalysts.

As the precursors of the Ni active component, as a rule, inorganic salts of this metal are used. It is established that for higher Ni dispersion using nickel nitrate or nickel acetate as a nickel metal precursor is preferred as against the use of nickel chloride or nickel formate [53]. In order to obtain a high dispersion state for Ni active components, the addition of organic agents such as poly(N-vinyl-2-pyrrolidone) (PVP) [54], citric acid [55], sorbitol or glucose [56] into impregnation solution is made. For example, the application of glucose additive allows decreasing of the average Ni particle size from 7.2 to 3.5 nm in 10 wt.%Ni/Al_2O_3 samples [56], while the use of poly(N-vinyl-2-pyrrolidone) leads to reduction of the average Ni particle size from 13.0 to 4.3 nm in 5 wt.%Ni/SBA-15 samples [54]. Catalysts prepared with PVP showed better stability in methane reforming. The presence of organic compounds controls the re-distribution of Ni species across the support and their sintering during the activation procedures, thus providing the stabilization of Ni nanoparticles of high dispersion and, consequently, high catalytic properties of materials.

Exploitation of the so-called “POSS nanotechnology” (POSS = polyhedral oligomeric silsesquioxanes) in which metal-containing silsesquioxanes are used as precursors for the preparation of nanomaterials has attracted attention as a tool

for synthesis of catalysts with novel properties and functionalities. This method of nanosized catalysts preparation has distinct advantage over traditional methods because the metal atoms remain highly dispersed throughout support [57–59]. The study of the Fe-, Cr-, Mg- and Al-containing silicas derived through controlled calcination of appropriate metallsilsesquioxanes showed that nearly homogenous metal dispersion could be achieved [60–62]. In the case of Cr- and Fe-containing silicas the small amount of oxide particles was additionally observed.

In this work we have expanded the POSS nanotechnology method for the preparation of $Ni/SiO_2/Ce_{0.5}Zr_{0.5}O_2$ catalysts. The peculiarity of the genesis of $Ni/SiO_2/Ce_{0.5}Zr_{0.5}O_2$ nanomaterials and their performance in the ATR of CH_4 were thoroughly studied. Using X-ray fluorescence spectroscopy, thermal analysis, N_2 adsorption, X-ray diffraction, high-resolution transmission electron microscopy and H_2 temperature-programmed reduction methods the textural, structural and redox properties of the prepared nanomaterials were examined in detail. The results were analyzed in comparison with those for Ni/SiO_2 and $Ni/Ce_{0.5}Zr_{0.5}O_2$ catalysts prepared by conventional method.

2. Experimental

2.1. Support and catalyst preparation

$Ce_{0.5}Zr_{0.5}O_2$ support was prepared by polymerizable complex method [44, 63]. Aqueous solutions of cerium nitrate $Ce(NO)_3 \cdot 6H_2O$ and zirconium oxychloride $ZrOCl_2 \cdot 8H_2O$ taken in the equimolar ratio were added to the solution of citric acid (CA) in ethylene glycol (EG) at 70 °C. Then ethylene diamine (ED) was mixed with this solution at 50 °C, and the mixture was kept at 70 °C until a highly viscous polymeric gel was formed. The molar ratio of the reagents (Ce + Zr):CA:EG:ED was 1:4:11:4. The obtained product was subjected to two-step calcination in air: at 300 °C for 4 h and at 600 °C for 4 h.

$Ni/SiO_2/Ce_{0.5}Zr_{0.5}O_2$ catalysts were prepared by deposition of Ni-POSS $[(C_4H_9)_7Si_7O_9(OH)O_2Ni]$ on the $Ce_{0.5}Zr_{0.5}O_2$ support. Different modes of deposition were applied: (1) single step deposition of Ni-POSS, (2) three steps deposition of Ni-POSS and (3) three steps deposition of Ni-POSS with intermediate calcination. The Ni/SiO_2 and $Ni/Ce_{0.5}Zr_{0.5}O_2$ samples were prepared by incipient wetness impregnation of support with aqueous solutions of nickel nitrate $Ni(NO_3)_2 \cdot 6H_2O$. All the prepared catalysts were calcined in air at 600 °C for 6 h.

2.2. Characterization of catalysts

Elemental composition of the catalysts was determined by X-ray fluorescence analysis in a spectrometer ARL PERFORM'X (Thermo Techno Scientific) with a Rh anode of the X-ray tube.

XRD analysis of the catalysts was carried out in an HZG-4C diffractometer (Freiberger Prazisionmechanik) with CoK_α radiation The phase composition was determined by X-ray diffraction (XRD) in the 2Theta angle range of 10–80 degrees. The phase identification was carried out using JCPDS database.

The BET specific surface area and porosity texture of support and catalyst samples were determined by nitrogen adsorption measurements at liquid nitrogen temperature with an automatic Micromeritics ASAP 2400 instrument. Before the measurements the samples were degassed at 150 °C for 4 h.

The Brunauer–Emmett–Teller (BET) and Barret–Joyner–Halenda (BJH) methods were applied for calculation of the specific surface area, pore volume and pore size distribution.

The thermal analysis (TA) (thermogravimetric (TG), differential thermogravimetric (DTG) and differential thermal analysis (DTA)) was carried out in a Netzsch STA 449C apparatus. Catalysts were tested over the temperature range from room temperature up to 900 °C at the heating rate of 10 °C/min in air.

The transmission electron microscopy (TEM) images of the catalysts were obtained in a JEM 2010 microscope (JEOL) operated at 200 kV. The structural resolution was 0.14 nm. The samples were deposited on a copper grid supporting a perforated carbon film. Local Energy Dispersive X-ray (EDX) microanalysis was made in an EDAX analyzer equipped with a Si (Li) detector with a resolution of 130 eV.

Hydrogen TPR studies were carried out in a flow quartz reactor with an i.d. of 5 mm. Samples of ca. 50 mg were loaded into the reactor, pre-treated in oxygen flow at 500 °C for 0.5 h and cooled down to room temperature. Then the gas stream was switched to $10\%H_2/Ar$. The reactor was heated at a rate of 10 °C/min to 800 °C. Hydrogen consumption was determined quantitatively by a thermal conductivity detector.

2.3. Catalytic activity tests

ATR experiments were carried out in a quartz flow reactor (i.d. = 14 mm) at ambient pressure, temperatures from 650 to 950 °C and a flow rate 200 mlN/min. The feed gas composition was CH_4 : H_2O : O_2 : He = 1 : 1 : 0.75 : 2. In experiments pure gases were used: 99.95% CH_4, 99.995% O_2 and 99.995% He. Water vapor was fed by dosing distilled water into an evaporator with a pump. Prior to each ATR experiment, the catalysts pretreated in 30%H_2/He flow (100 mlN/min) at 800 °C for 2 h.

To minimize local catalysts overheating, the loaded catalyst sample (0.5 g, fraction 0.25–0.50 mm) was diluted by an inert material having higher heat conductivity – 1.5 g of β-SiC of the same fraction. Analysis of the initial gas mixture and the reaction products was performed in a QMS 300 mass-spectrometric gas analyzer (Stanford Research Systems) using peak intensity calibrations obtained with model gas mixtures.

Yields of H_2 and CO were determined as percent of the amounts of products produced by the reaction from maximally possible amounts, using the following equations:

$Y_{H2} = 100\% \cdot V_{H2out}/(2V_{CH4in} + V_{H2Oin})$, where

Y_{H2} is a yield of H_2, %;

V_{H2out} is a molar rate of H_2 at the reactor outlet, mol/min;

V_{CH4in} is a molar rate of CH_4 introduced into the reactor, mol/min;

V_{H2Oin} is a molar rate of H_2O fed into the reactor, mol/min; and

$Y_{CO} = 100\% \cdot V_{COout}/V_{CH4in}$, where

Y_{CO} is a yield of CO, %

V_{COout} is a molar rate of CO at the reactor outlet, mol/min;

V_{CH4in} is a molar rate of CH_4 introduced into the reactor, mol/min.

The relative experimental error in the determination of methane conversion and product yields did not exceed 10%.

3. Results and discussion

*3.1 Characterization of the catalyst*s

Table 1 shows the sample formula and chemical composition of prepared catalysts. It can be noted that according to actual chemical composition of samples, the Si/Ni atomic ratio in the Ni/SiO_2/$Ce_{0.5}Zr_{0.5}O_2$ catalysts differ from Si/Ni atomic ratio in Ni-POSS (namely, 3 vs. 7). Theoretically the Ni content should be lower (ca. 4%) while the Si content should be higher (ca. 13%). The deviation of the obtained values from nominal specified values can be connected with loss of Si-organic fragments during thermal treatment because of its high volatility [64].

To study the peculiarity of Ni catalyst genesis, the samples dried at 120 °C were characterized by the thermal analysis. The typical TG, DTG and DTA curves of dried samples are shown in Fig. 1. When the dried Ni/SiO_2/$Ce_{0.5}Zr_{0.5}O_2$-1 sample was heated from the room temperature up to 900 °C (Fig. 1, upper left quarter), there were three pronounced exo-effects at 200, 300 and 445 °C on the DTA curve. Meanwhile, it has lost 6.5 wt.% at 150–250 °C, 6.5 wt.% at 250–400 °C and 1.6 wt.% at 400–500 °C. The origin of the weight loss is the decomposition of supported Ni-POSS. The results of TA suggest that it is a multi-stage process, which is accompanied by organic group oxidation with release of carbon oxides and water. The thermal degradation of supported Ni-POSS is completed at 600 °C, and this value of temperature was applied for the calcination of dried Ni/SiO_2/$Ce_{0.5}Zr_{0.5}O_2$ samples.

Table 1
Sample formula and chemical composition of Ni-based catalysts

Sample formula	Description	Chemical composition, wt.%			
		Ni	Si	Ce	Zr
Ni precursor: Nickel (II) - HeptaisobutylPOSS [$(C_4H_9)_7Si_7O_9(OH)O_2Ni$]					
Ni/SiO_2/$Ce_{0.5}Zr_{0.5}O_2$-1	single step deposition of Ni-POSS	5.9	8.7	33.3	22.0
Ni/SiO_2/$Ce_{0.5}Zr_{0.5}O_2$-2	three steps deposition of Ni-POSS	6.0	8.5	32.3	22.0
Ni/SiO_2/$Ce_{0.5}Zr_{0.5}O_2$-3	three steps deposition of Ni-POSS with intermediate calcination	6.2	9.1	33.1	21.6
Ni precursor: Nickel (II) nitrate hexahydrate [$Ni(NO_3)_2 \cdot 6H_2O$]					
Ni/SiO_2		6.1	43.0	-	-
Ni/$Ce_{0.5}Zr_{0.5}O_2$		6.1		47.6	28.9

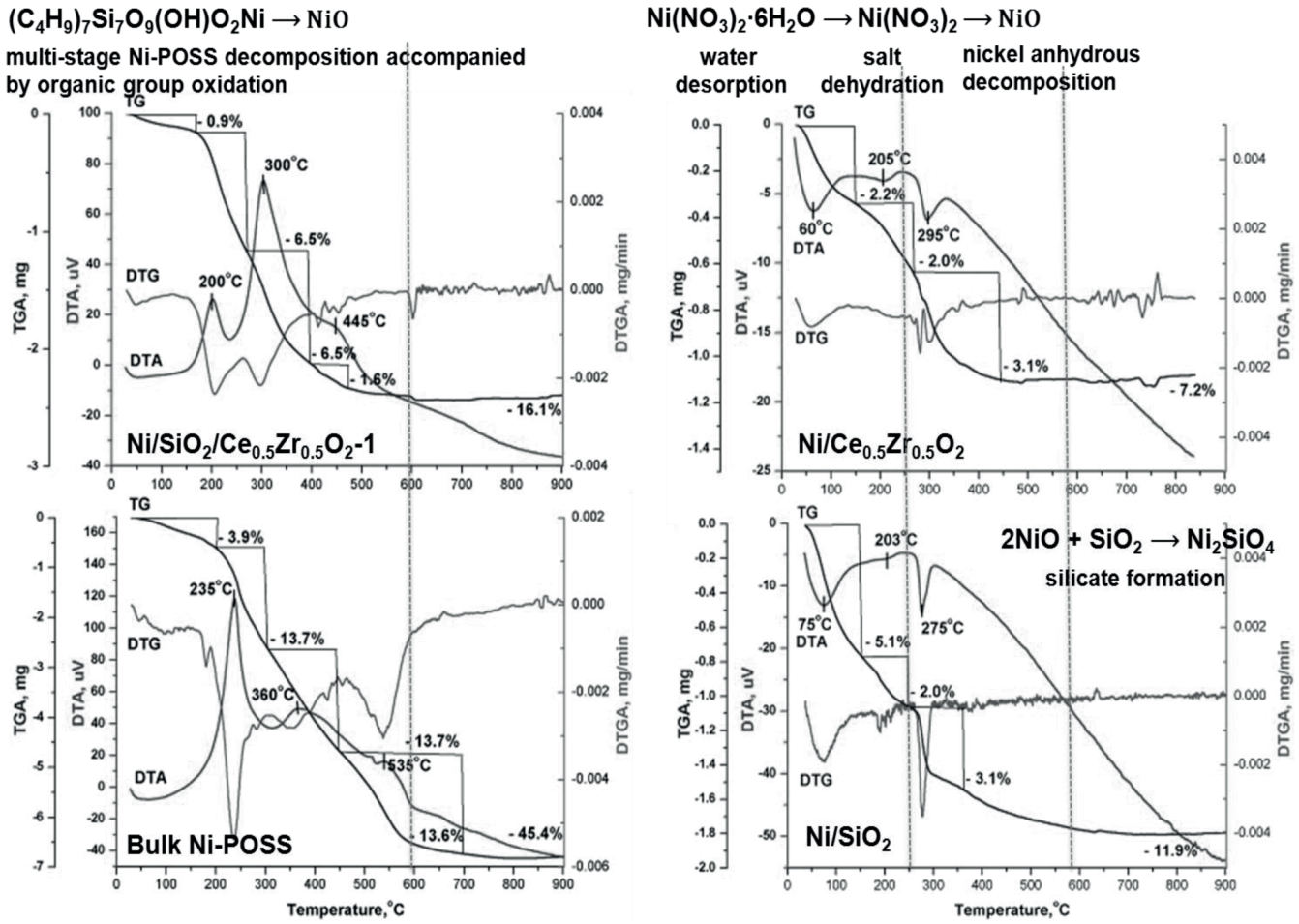

Fig. 1. Thermal degradation of Ni precursors: DTA/TGA of catalysts dried at 120 °C.

It can be also noted that the Ni-POSS thermal degradation behavior in supported $Ni/SiO_2/Ce_{0.5}Zr_{0.5}O_2$ and bulk samples is quite similar (Fig. 1, upper and lower left quarters). For both samples three exo-effects accompanied by weight loss are observed. However, for supported Ni-POSS the peak distribution is inverted with a considerable increase of peak 2 in relation to peak 1. This indicates that the thermooxidative degradation of supported Ni-POSS has a more intensive mode in the second stage (ca. 300 °C) while that for bulk Ni-POSS is more pronounced at the first stage (ca. 235 °C).

In addition, the supported Ni-POSS differs by shifting of observed exo-effects in the low-temperature region (200 vs. 235 °C, 300 vs. 360 °C and 445 °C vs. 535 °C). The decrease of temperature of Ni-POSS decomposition in the supported state is probably related to variable valence of cerium (Ce^{3+}/Ce^{4+}) in $Ce_{0.5}Zr_{0.5}O_2$ support that promotes the reaction of oxidation of organic compounds [65].

In contrast to the degradation of supported and bulk Ni-POSS that goes with the exo-effects, the decomposition of supported Ni nitrate is accompanied by endo-effects (Fig. 1, upper and lower right quarters). The DTA peaks (for example, for $Ni/Ce_{0.5}Zr_{0.5}O_2$ – at 60 °C, 205 °C and 295 °C) are closely corresponding to the weight changes observed on the TGA curve. The weight loss event in the temperature range 50–250 °C is characterized by the endothermic peaks and can be attributed to: (i) desorption of physically bonded water; (ii) dehydration process of the salt precursors of Ni metallic components with formation of the $Ni(NO_3)_2$ anhydrous material. The next weight loss event is in the temperature range 250–350 °C and corresponds to the Ni anhydrous material decomposition into nitrogen oxides and NiO, that is in the good accordance with published data for bulk Ni nitrate hydrates [66–68]. The degradation of supported Ni nitrate salt is completed at 450 and 550 °C for $Ce_{0.5}Zr_{0.5}O_2$ and SiO_2 supports, respectively. In addition, for the Ni/SiO_2 sample, formation of the Ni_2SiO_4 cannot be excluded after rising the temperature up to 900 °C [69].

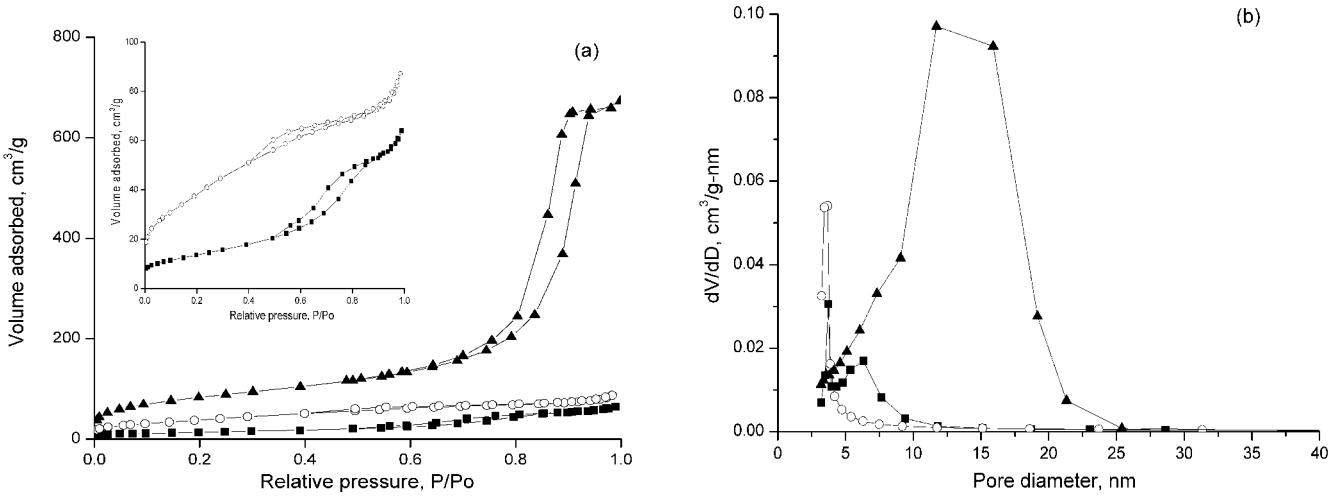

Fig. 2. N_2 sorption isotherms (a, lower volume adsorbed range is shown at larger scale on the inset) and BJH pore size distributions (b) derived from desorption branches of Ni-based catalysts: (○) – $Ni/SiO_2/Ce_{0.5}Zr_{0.5}O_2$-1, (■) – $Ni/Ce_{0.5}Zr_{0.5}O_2$, (▲) – Ni/SiO_2.

Table 2
Textural properties of Ni-based catalysts

Sample formula	Textural data		
	S_{BET}, m^2/g	V_{pore}, cm^3/g	D_{pore}, nm
$Ni/SiO_2/Ce_{0.5}Zr_{0.5}O_2$-1	140	0.13	3.9
$Ni/SiO_2/Ce_{0.5}Zr_{0.5}O_2$-2	165	0.15	3.7
$Ni/SiO_2/Ce_{0.5}Zr_{0.5}O_2$-3	65	0.09	5.5
Ni/SiO_2	300	1.04	13.7
$Ni/Ce_{0.5}Zr_{0.5}O_2$	50	0.10	8.1

The N_2 adsorption-desorption isotherms, pore size distributions and the textural properties of the samples are given in Fig. 2 and Table 2, respectively. It is shown (Table 2) that introduction of the Ni-POSS into the $Ce_{0.5}Zr_{0.5}O_2$ support (S_{BET} = 65 m^2/g) and further high-temperature calcination of the samples lead to an increase of S_{BET} by ~ 2–2.5 times in the case of $Ni/SiO_2/Ce_{0.5}Zr_{0.5}O_2$-1 and $Ni/SiO_2/Ce_{0.5}Zr_{0.5}O_2$-2 samples. In the case of three steps deposition of Ni-POSS with intermediate calcination, the S_{BET} of support and catalyst are equal. The average pore diameter decreases during Ni-POSS deposition on the mixed oxide support (D_{pore} = 8.0 nm) and becomes in the range of ~ 3.7–5.5 nm. Impregnation of the $Ce_{0.5}Zr_{0.5}O_2$ and SiO_2 (S_{BET} = 325 m^2/g) supports with the aqueous solutions of Ni precursor and further calcination leads to a decrease of S_{BET} by ~ 20% and ~ 5%, respectively. The average pore diameter practically does not change during Ni nitrate salt deposition on the supports.

The N_2 adsorption-desorption isotherms, pore size distributions and the textural properties of the samples are given in Fig. 2 and Table 2, respectively. It is shown (Table 2) that introduction of the Ni-POSS into the $Ce_{0.5}Zr_{0.5}O_2$ support (S_{BET} = 65 m^2/g) and further high-temperature calcination of the samples lead to an increase of S_{BET} by ~ 2–2.5 times in the case of $Ni/SiO_2/Ce_{0.5}Zr_{0.5}O_2$-1 and $Ni/SiO_2/Ce_{0.5}Zr_{0.5}O_2$-2 samples. In the case of three steps deposition of Ni-POSS with intermediate calcination, the S_{BET} of support and catalyst are equal. The average pore diameter decreases during Ni-POSS deposition on the mixed oxide support (D_{pore} = 8.0 nm) and becomes in the range of ~ 3.7–5.5 nm. Impregnation of the $Ce_{0.5}Zr_{0.5}O_2$ and SiO_2 (S_{BET} = 325 m^2/g) supports with the aqueous solutions of Ni precursor and further calcination leads to a decrease of S_{BET} by ~ 20% and ~ 5%, respectively. The average pore diameter practically does not change during Ni nitrate salt deposition on the supports.

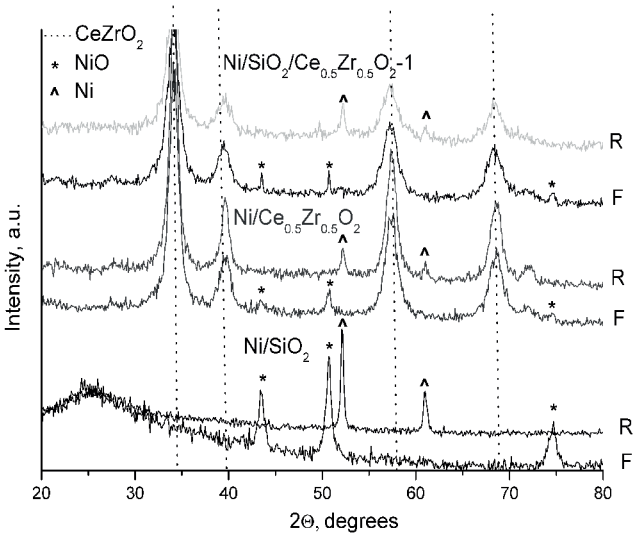

Fig. 3. X-ray diffraction patterns of fresh (F) and reduced (R) Ni-based catalysts.

The N_2 adsorption on $Ni/SiO_2/Ce_{0.5}Zr_{0.5}O_2$ and $Ni/Ce_{0.5}Zr_{0.5}O_2$ catalysts shows a type IV isotherm (Fig. 2), H3-type hysteresis loop according to the IUPAC classification and capillary condensation step at relative pressure above 0.4, which are characteristic for mesoporous materials [70]. The Ni/SiO_2 catalyst is characterized by a type IV isotherm with H1-type hysteresis loop at relative pressure above 0.8, that indicates the existence of mainly textural mesoporosity [71].

The BJH analysis of desorption isotherms revealed that the $Ni/SiO_2/Ce_{0.5}Zr_{0.5}O_2$ catalysts exhibited narrow pore size distributions with a mean pore size of 3.7–5.5 nm. The $Ni/Ce_{0.5}Zr_{0.5}O_2$ and, especially, Ni/SiO_2 samples showed a broader pore size distributions with larger average pore diameters (Fig. 2, Table 2).

The surface area of the $Ni/SiO_2/Ce_{0.5}Zr_{0.5}O_2$ catalysts which have different deposition strategy decreased from 140 m^2/g in $Ni/SiO_2/Ce_{0.5}Zr_{0.5}O_2$-1 to 65 m^2/g in $Ni/SiO_2/Ce_{0.5}Zr_{0.5}O_2$-3 as a consequence of the increasing of number of deposition-calcination steps. In overall, the value of S_{BET} increases in the order: $Ni/Ce_{0.5}Zr_{0.5}O_2$ < $Ni/SiO_2/Ce_{0.5}Zr_{0.5}O_2$ < Ni/SiO_2, that may have effect on the active component dispersion in the support matrix. The higher S_{BET} value of $Ni/SiO_2/Ce_{0.5}Zr_{0.5}O_2$ samples in comparison with those of $Ni/Ce_{0.5}Zr_{0.5}O_2$ is likely connected with the presence of amorphous SiO_2 (~20 wt.%) in the catalyst composition, which is characterized by higher value of S_{BET}. This tendency is typical for $Ce_{0.5}Zr_{0.5}O_2$-SiO_2 composite materials [72].

According to the XRD data (Fig. 3), the ceria-based cubic solid solution (JCPDS 34-0394) and NiO (JCPDS 44-1159) are main phases in the fresh $Ni/SiO_2/Ce_{0.5}Zr_{0.5}O_2$ and $NiCe_{0.5}Zr_{0.5}O_2$ catalysts after calcination at 600 °C. The characterization by XRD of fresh catalysts prepared using different modes of Ni-POSS deposition does not allow to find differences among them. In the Ni/SiO_2 catalyst the NiO phase and SiO_2 amorphous phase are observed. The reduction of samples in the hydrogen at 800 °C as a typical stage of catalyst activation for ATR of CH_4 leads to an expected transformation of NiO into metallic Ni phase (Fig. 3).

The average crystallite sizes of active component phases were estimated by the Debye-Scherrer equation and are presented in Table 3. The obtained values of NiO and Ni average particle size lie in the typical range of such values for Ni supported on SiO_2, CeO_2-ZrO_2 or SiO_2-CeO_2-ZrO_2 [72–74]. For the fresh samples, data show that the NiO particles of equal mean size form in all $Ni/SiO_2/Ce_{0.5}Zr_{0.5}O_2$ catalysts regardless of the deposition mode used in their synthesis. The results also demonstrate that for fresh samples average size of NiO particles increases from 18 to 30 nm in the following order of catalysts: Ni/SiO_2 < $Ni/Ce_{0.5}Zr_{0.5}O_2$ < $Ni/SiO_2/Ce_{0.5}Zr_{0.5}O_2$ (Table 3). It is noted that there is no straightforward correlation between the value of S_{BET} and the average NiO (or Ni) particle size for the studied samples.

In the catalysts after reduction the average size of Ni particles is equal ~ 25 nm in all studied samples with the exception of $Ni/SiO_2/Ce_{0.5}Zr_{0.5}O_2$-3 (Table 3). The average size of Ni-containing particles in reduced $Ni/SiO_2/Ce_{0.5}Zr_{0.5}O_2$ samples is comparable with or lower than those obtained for fresh catalysts. So, according to the XRD data, the nanoparticles were stable against sintering during high-temperature activation at 800 °C in the reducing medium. It is known that the strong interaction between metal and support increases the dispersion of Ni-containing species and decreases their particle size, that can be realized in the reduced $Ni/SiO_2/Ce_{0.5}Zr_{0.5}O_2$-3 catalyst. On the other hand, some agglomeration of Ni-containing particles is observed in the reduced $Ni/Ce_{0.5}Zr_{0.5}O_2$ and Ni/SiO_2 catalysts compared to their fresh states.

Table 3
XRD data: average size of Ni-containing particles for fresh (F) and reduced (R) Ni-based catalysts

Sample formula	Average particle size, nm	
	NiO (F)	Ni (R)
$Ni/SiO_2/Ce_{0.5}Zr_{0.5}O_2$-1	30	24
$Ni/SiO_2/Ce_{0.5}Zr_{0.5}O_2$-2	30	24
$Ni/SiO_2/Ce_{0.5}Zr_{0.5}O_2$-3	30	15
Ni/SiO_2	18	23
$Ni/Ce_{0.5}Zr_{0.5}O_2$	21	26

TEM data illustrate that support of the fresh and reduced $Ni/SiO_2/Ce_{0.5}Zr_{0.5}O_2$ catalysts consists of SiO_2 particles about 500 nm in size and agglomerates of $Ce_{0.5}Zr_{0.5}O_2$ crystallites within 5–10 nm in size (Figs. 4a, d). There are intimate contacts between SiO_2 and $Ce_{0.5}Zr_{0.5}O_2$: the $CeZeO_2$ particles (2–10 nm) were found on the surface of SiO_2 particles (up to 500 nm), while $Ce_{0.5}Zr_{0.5}O_2$ crystallites are partly covered by SiO_2 (Fig. 4b). The NiO particles of 1–2 nm in size in the fresh catalysts (Fig. 4c) and Ni particles of 3–4 nm in size in the reduced catalysts (Fig. 4f) are mainly found on SiO_2. According to the EDX data, highly dispersed Ni species are present on/in the $Ce_{0.5}Zr_{0.5}O_2$ region of support (Figs. 4b, e). In addition, the large

Ni-containing particles (up to 50–100 nm in size) are also observed.

Further, using TEM for the comparison of nanostructure of Ni/SiO_2 and $Ni/Ce_{0.5}Zr_{0.5}O_2$ shows that for both fresh catalysts large NiO particles are observed on the supports: the NiO particle sizes are 10–50 nm for SiO_2 (Figs. 5a, 4b) and 10–100 nm for $Ce_{0.5}Zr_{0.5}O_2$ (Fig. 5d). According to the EDX data, in the $Ni/Ce_{0.5}Zr_{0.5}O_2$ catalyst the Ni-containing species are also present on $Ce_{0.5}Zr_{0.5}O_2$ in the highly dispersed form, or they are included in the $Ce_{0.5}Zr_{0.5}O_2$ structure (Fig. 5e). In contrast to $Ni/SiO_2/Ce_{0.5}Zr_{0.5}O_2$ catalysts, in the case of Ni/SiO_2 and $Ni/Ce_{0.5}Zr_{0.5}O_2$ samples after reduction, formation of the Ni agglomerated particles occurs (Fig. 5c). The particle sizes increase up to 100 nm for Ni/SiO_2 and up to 500 nm for $Ni/Ce_{0.5}Zr_{0.5}O_2$. Nevertheless, EDX data show that dispersed Ni species are retained in the reduced $Ni/Ce_{0.5}Zr_{0.5}O_2$ catalyst (Fig. 5f).

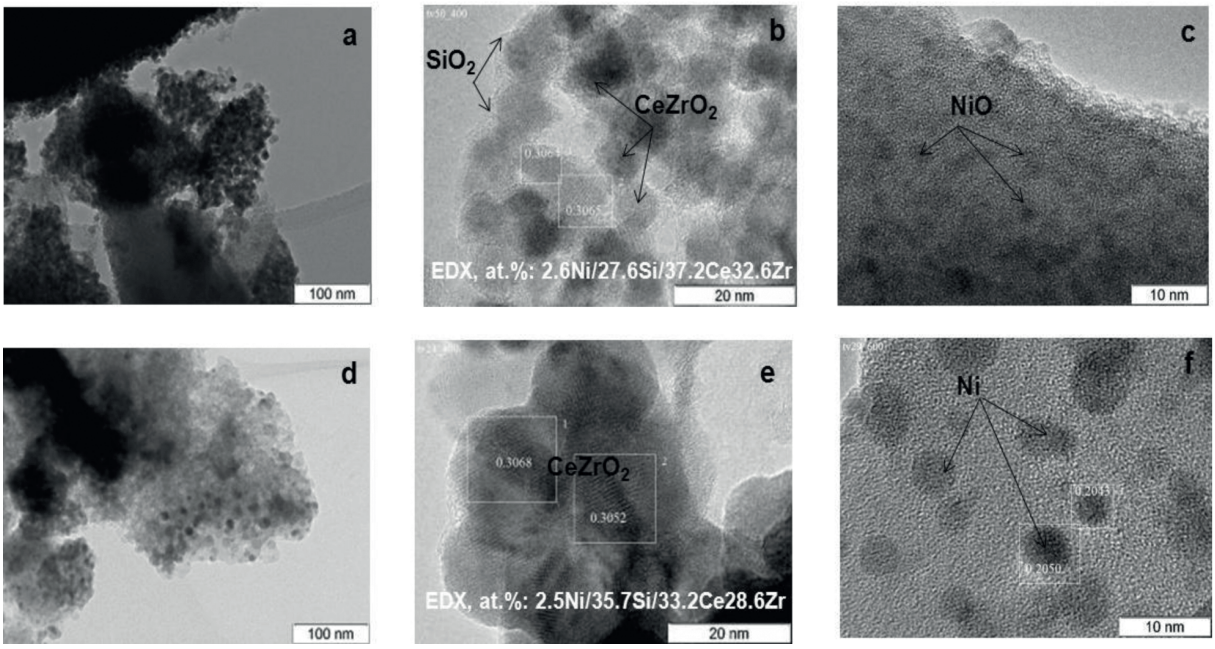

Fig. 4. TEM images of fresh (a-c) and reduced (d-f) $Ni/SiO_2/Ce_{0.5}Zr_{0.5}O_2$-1 catalysts.

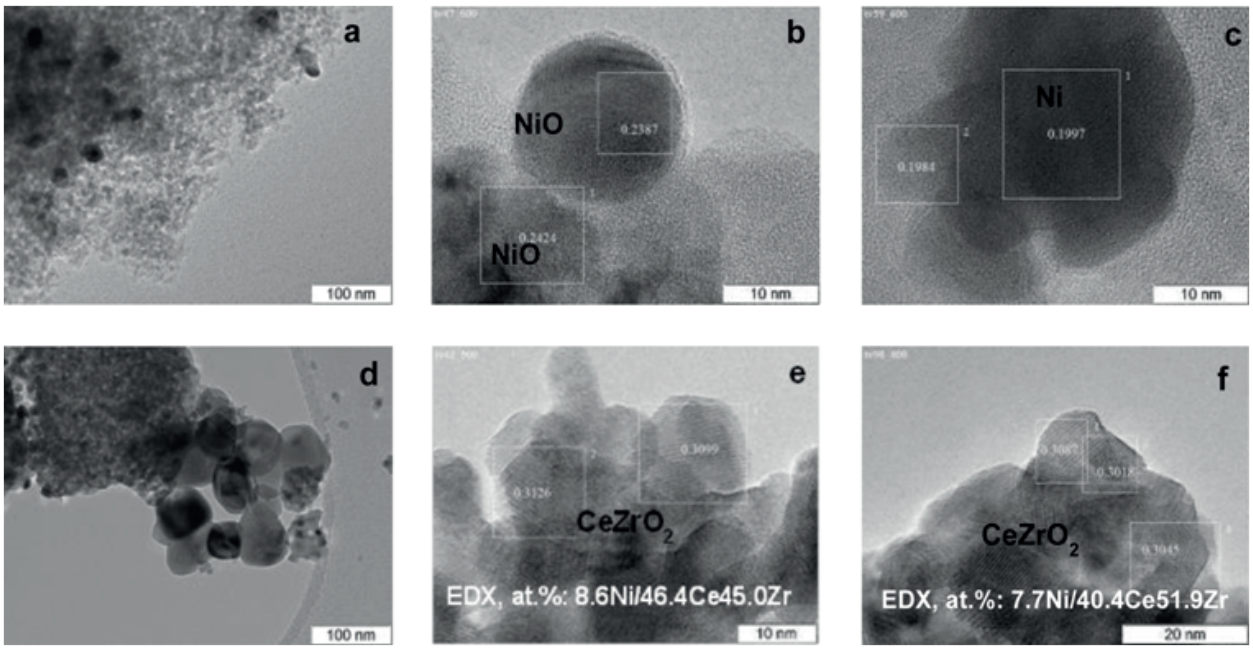

Fig. 5. TEM images of: fresh (a, b) and reduced (c) Ni/SiO_2 catalysts; fresh (d, e) and reduced (f) $Ni/Ce_{0.5}Zr_{0.5}O_2$ catalysts.

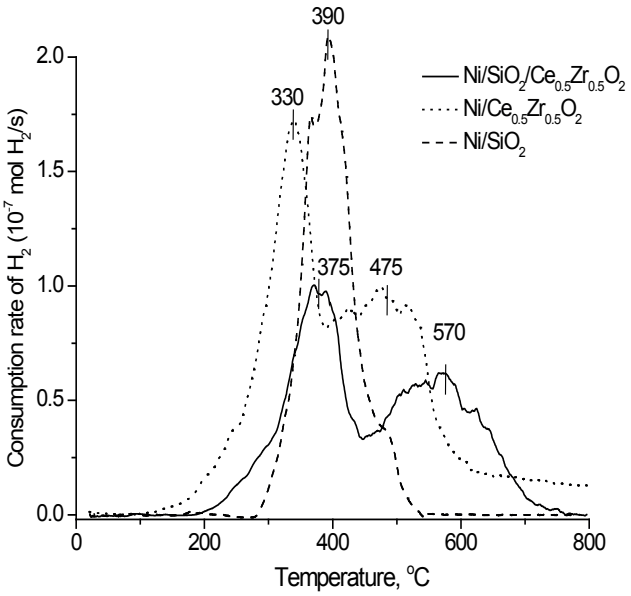

Fig. 6. H_2-TPR profiles of Ni-based catalysts.

The size of NiO and Ni particles detected on the support by HRTEM (Figs. 4 and 5) does not exactly correspond to the average particle size estimated by XRD. A plausible reasons are that:

i) the portion of particles have dimensions below the detection limit of XRD (ca. 3 nm);

ii) big Ni-containing particles is polycrystalline solid;

iii) wide Ni particle size distribution with a maximum at 20–30 nm takes place.

The H_2-TPR profiles associated with the studied Ni-based catalysts are given in Fig. 6. In particular, it can be seen that all the $Ni/SiO_2/Ce_{0.5}Zr_{0.5}O_2$ catalysts present two hydrogen consumption peaks with the temperature maxima T_1 in the range 350–380 °C and T_2 in the range 560–570 °C (Table 4), which can be assigned to reduction of NiO species with weak and intimate metal-support interaction, respectively [75]. While the maximum temperature of peaks is not very different for $Ni/SiO_2/Ce_{0.5}Zr_{0.5}O_2$ catalysts, the peak distribution is changed. As follows data in Table 4, some increase of peak 2 in relation to peak 1 (from 0.6 to 1) is observed in the following order of the samples: $Ni/SiO_2/Ce_{0.5}Zr_{0.5}O_2$-1 < $Ni/SiO_2/Ce_{0.5}Zr_{0.5}O_2$-2 < $Ni/SiO_2/Ce_{0.5}Zr_{0.5}O_2$-3. The increase of peak 2 intensity suggests an increase of the fraction of species with strong metal-support interaction. The metal-support interaction becomes stronger at the application of intermediate calcination during Ni-POSS deposition.

NiO bulk sample is known to exhibit a single reduction peak in H_2-TPR curve, whose position depends on the experimental conditions, for example, ca. 330 °C [76], 370 °C [77] or 530 °C [75]. In contrast, the reduction of supported NiO led to the appearance of several peaks in the H_2-TPR profile. Usually this is assigned to different forms of metal–support interaction [75, 78, 79]. It is suggested [80] that higher NiO reduction temperature can be due to the presence of particles with higher dispersion, interacting stronger with the support, while the lower reduction temperature can be related to larger particles with a lower strength of interaction with the support (temperature of reduction closer to the pure NiO sample). The highly dispersed Ni species (1–2 nm) and large Ni-containing particles (up to 50–100 nm in size) were observed by HR-TEM, which is consistent with two peaks in the H_2-TPR experiments and indicative of realization of both weak and strong metal interaction with the support.

The profile of H_2-TPR curve similar to those of $Ni/SiO_2/Ce_{0.5}Zr_{0.5}O_2$ samples is obtained for the $Ni/Ce_{0.5}Zr_{0.5}O_2$ catalyst (Fig. 6). However, in this case the maxima of hydrogen consumption peaks shift to the low-temperature region (Table 4), that can be assigned to the weakening of metal-support interaction and increase of NiO particle size. H_2-TPR profile associated with the Ni/SiO_2 catalyst shows hydrogen consumption peak with a maximum T_1 at 390 °C and feebly marked shoulder at 475 °C. Usually such peak was assigned to the reduction of "free state" NiO bearing weak interaction with the support [28]. It is noted that value of H_2/Ni molar ratio is over-stoichiometric (higher than 1) for both $Ni/SiO_2/Ce_{0.5}Zr_{0.5}O_2$ and $Ni/Ce_{0.5}Zr_{0.5}O_2$ catalysts, which can be associated with the additional reduction of $Ce_{0.5}Zr_{0.5}O_2$ solid solution [78, 81].

Hence, the reduction of Ni species in the supported nickel catalysts takes place in a broad temperature range from 250 °C to 750 °C and the Ni^{2+} reducibility is affected by support composition and catalyst preparation technique. The presence of H_2 consumption at temperatures above 500 °C suggests the existence of Ni species with strong metal-support interaction. As follows from the ratio of area of peak 2 to that of peak 1 (Table 4), the content of such type of Ni species increases in the following order of catalysts: Ni/SiO_2 << $Ni/Ce_{0.5}Zr_{0.5}O_2$ ≤ $Ni/SiO_2/Ce_{0.5}Zr_{0.5}O_2$ and with the application of intermediate calcination during Ni-POSS deposition. Conclusions derived from the H_2-TPR profiles are in good agreement with those proposed from the XRD and TEM results.

Table 4
Data obtained from H_2-TPR

Sample formula	Temperature of peak maximum, °C		H_2/Ni molar ratio
	T_1	T_2	
$Ni/SiO_2/Ce_{0.5}Zr_{0.5}O_2$-1	355	570	1.5
$Ni/SiO_2/Ce_{0.5}Zr_{0.5}O_2$-2	355	565	1.5
$Ni/SiO_2/Ce_{0.5}Zr_{0.5}O_2$-3	375	570	1.3
Ni/SiO_2	390	480	1.1
$Ni/Ce_{0.5}Zr_{0.5}O_2$	330	475	1.8

3.2. Catalytic tests

The catalytic behavior of nickel catalysts in the ATR of CH_4 was comparatively studied. Figure 7 demonstrates the characteristic temperature dependences of methane conversion and hydrogen yield: it is seen that generally these values increase with temperature. This trend is most marked for the $Ni/SiO_2/Ce_{0.5}Zr_{0.5}O_2$-1 catalyst. As seen from Fig. 7, the catalyst efficiency is also substantially influenced by the Ni-POSS deposition mode. The conversion of CH_4 and yields of H_2 and CO are much higher in case of the single step deposition: at 850 °C the H_2 yield of was ~ 75% for the $Ni/SiO_2/Ce_{0.5}Zr_{0.5}O_2$-2, while the H_2 yield of ~95% was found for the $Ni/SiO_2/Ce_{0.5}Zr_{0.5}O_2$-1. The $Ni/SiO_2/Ce_{0.5}Zr_{0.5}O_2$-3 catalyst is not active in temperature range lower than 900 °C (Fig. 7). So the multiple deposition and intermediate calcination impair the catalyst performance. It is probably caused by encapsulation of Ni species in the SiO_2 matrix, which is accompanied by the lower S_{BET} and V_{pore}, but higher D_{pore} values (Table 2), compared to the two preceding samples $Ni/SiO_2/Ce_{0.5}Zr_{0.5}O_2$-1,2. Other differences in the structural and redox properties of these series of catalysts were revealed by XRD, TEM and H_2-TPR, which is discussed further in the text.

The summarized comparison of catalyst efficiencies in the ATR of CH_4 is shown in Table 5 where CH_4 conversion, yields of H_2 and CO and H_2/CO ratio are given as a function of different catalyst compositions. Analysis of these data shows that use of the metal-POSS precursor can provide formation of the active materials for ATR of CH_4: the ex-Ni-POSS catalysts have performance in ATR of CH_4 which is comparable with or better than those presented by the traditionally prepared catalysts. The $Ni/SiO_2/Ce_{0.5}Zr_{0.5}O_2$-1 catalyst prepared by one-step Ni-POSS deposition gives the highest H_2 yield of 80% at T = 800 °C.

As it was shown above (Fig. 3, Table 3), all the $Ni/SiO_2/Ce_{0.5}Zr_{0.5}O_2$ samples after activation in the reducing medium at 800 °C have similar XRD patterns (CeO_2-based solid solution and metallic Ni) but different average Ni particle size: for the $Ni/SiO_2/Ce_{0.5}Zr_{0.5}O_2$-1 and $Ni/SiO_2/Ce_{0.5}Zr_{0.5}O_2$-2 it is 25 nm, while for $Ni/SiO_2/Ce_{0.5}Zr_{0.5}O_2$-3 it is 15 nm. In addition, differences in the catalytic performance can be correlated with H_2-TPR behaviors of $Ni/SiO_2/Ce_{0.5}Zr_{0.5}O_2$ samples (Fig. 6, Table 4). The increase of a portion of difficultly reduced Ni^{2+} species, as well as the increase of T_1 value corresponding to the weak interaction of Ni^{2+} species with support, are found for $Ni/SiO_2/Ce_{0.5}Zr_{0.5}O_2$-3 catalyst, that are expected to have detrimental effect on its activity in the ATR of CH_4. It was shown that the increase of both the reducibility of NiO and the Ni^o surface dispersion resulted in a rise of CH_4 conversion [79, 80, 82]. Conversely, it was also concluded that NiO dispersed without strong interaction with the support had a high performance in methane partial oxidation, while in case of NiO dispersed with strong interaction between it and the support the catalyst had a high stability in autothermal reforming in the upper temperature range [83]. This seems to combine, on the one hand, a high reducibility, which is key factor of high activity and stability against active component oxidation, and, on the other hand, a strong metal-support interaction, that is assurance of stability against sintering and coking, so the modification of catalyst in which Ni have strong interaction with support by noble metals is useful strategy.

It can be proposed that multiple deposition-calcination steps promote the realization of strong metal-support interaction up to formation highly dispersed nickel silicate species. After reduction such species can remain in the state of Ni-Si-O, which decreases the number of active sites, resulting in the lower activity of $Ni/SiO_2/Ce_{0.5}Zr_{0.5}O_2$-3 compared with other catalysts. This situation is common with those for Ni- and Rh-based catalyst supported on La_2O_3 [44] which provides worse performance in ATR of CH_4 in comparison with catalyst supported on $Ce_{1-x}Zr_xO_y$ and $Ce_{1-x}Gd_xO_y$. The poorest or non-existent catalytic activity in the temperature range up to 850–900 °C was connected with formation of stable to reduction mixed oxides (e.g. $LaNiO_3$ and $LaRhO_3$ species).

According to the published data [72, 84], Ni/SiO_2 catalyst had high initial activity but deactivated rapidly, while the stability of Ni/CeO_2-ZrO_2/

Table 5
Comparison of catalytic activity of different catalysts in ATR of CH_4 at 850 °C

Sample formula	Conversion of CH_4, %	Yield of H_2, %	Yield of CO, %	H_2/CO ratio
$Ni/SiO_2/Ce_{0.5}Zr_{0.5}O_2$-1	100	96	96	3.0
$Ni/SiO_2/Ce_{0.5}Zr_{0.5}O_2$-2	100	74	66	3.4
$Ni/SiO_2/Ce_{0.5}Zr_{0.5}O_2$-3	14	0	15	0.
Ni/SiO_2	100	87	73	3.5
$Ni/Ce_{0.5}Zr_{0.5}O_2$	65	59	53	3.3

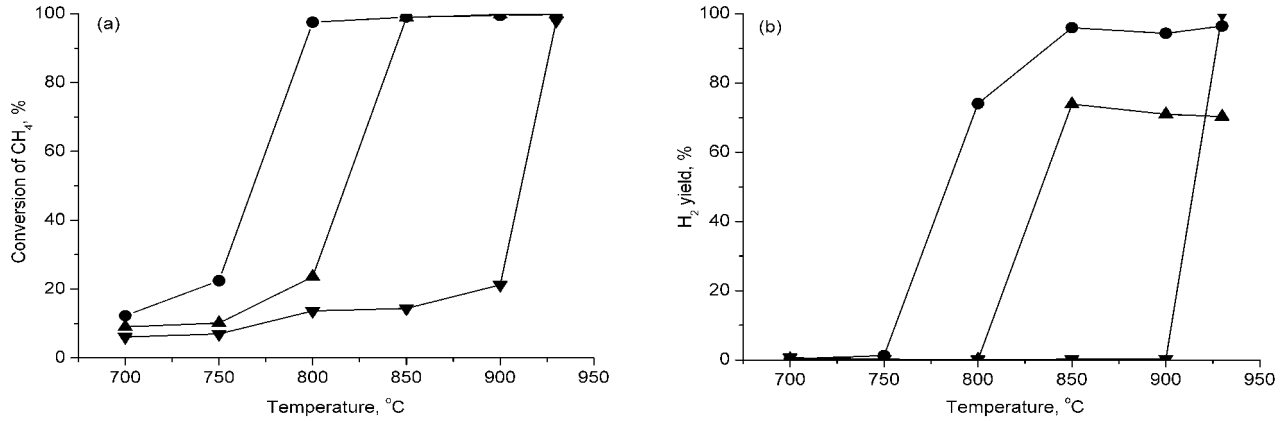

Fig. 7. Catalytic activity of $Ni/SiO_2/Ce_{0.5}Zr_{0.5}O_2$-1 (●), $Ni/SiO_2/Ce_{0.5}Zr_{0.5}O_2$-2 (▲) and $Ni/SiO_2/Ce_{0.5}Zr_{0.5}O_2$-3 (▼) catalysts in ATR of CH_4: (a) conversion of CH_4 vs. temperature, (b) H_2 yield vs. temperature.

SiO_2 catalysts was enhanced greatly. The increase in the reducibility and oxygen transfer ability of the support were believed to be the main reasons for the superior performance of $Ni/Ce_{0.5}Zr_{0.5}O_2$-SiO_2 sample as compared to Ni/SiO_2 catalyst in the ATR of CH_4 [84]. In our case the performance of $Ni/SiO_2/Ce_{0.5}Zr_{0.5}O_2$-2 and Ni/SiO_2 catalysts in ATR of CH_4 is close to each other. It is expected that the additional differences in catalytic activity will become apparent during prolonged time on stream, resulting from the differences in metal–support interaction, which will be a topic of further study.

$Ni/SiO_2/Ce_{0.5}Zr_{0.5}O_2$ catalysts were prepared by deposition of novel metal-POSS [Nickel (II) - HeptaisobutylPOSS $(C_4H_9)_7Si_7O_9(OH)O_2Ni$] on $Ce_{0.5}Zr_{0.5}O_2$ support with following calcination and reduction stages of activation. As a result of a multi-stage process of Ni-POSS decomposition proceeding in a temperature range 200–600 °C the NiO nanoparticles with mean size of 30 nm were stabilized in the support matrix. The nanoparticles were stable against sintering during high-temperature activation at 800 °C in reducing medium. The structural, redox and, especially, textural properties of $Ni/SiO_2/Ce_{0.5}Zr_{0.5}O_2$ catalysts were regulated by deposition mode. $Ni/SiO_2/Ce_{0.5}Zr_{0.5}O_2$ catalyst prepared by one-step Ni-POSS deposition gives the higher H_2 yield in ATR of CH_4 than those prepared by multiple deposition, which may be caused by a decrease of a portion of difficultly reduced Ni^{2+} species. The achieved value of H_2 yield 80% at 800 °C confirms that ex-Ni-POSS catalysts have good potential for hydrogen production by the ATR of CH_4.

Acknowledgements

Authors are grateful to Dr. V.A. Ushakov, Mrs. G.S. Litvak, Mrs. T.Ya. Efimenko and Dr. E.Yu. Gerasimov for their assistance with catalyst characterization. The presented research was initiated by the European Union 7th Framework Programme (FP7/2007-2013) under Grant Agreement No. 262840 (Project DEMCAMER) and has received funding from Russian Academy of Sciences and Federal Agency of Scientific Organizations (project № 0303-2016-0004).

References

[1]. N.Z. Muradov, T.N. Veziroglu, Int. J. Hydrogen Energy 33 (2008) 6804–6839. DOI: 10.1016/j.ijhydene.2008.08.054

[2]. J. Nowotny, N.T. Veziroglu, Int. J. Hydrogen Energy 36 (2011) 13218–13224. DOI: 10.1016/j.ijhydene.2011.07.071

[3]. C.C. Cormos, L. Petrescu, A.M. Cormos, Proceedings 24 European Symposium Computer Aided Process Engineering, Budapest, Hungary (2014) 1082–1086.

[4]. I. Dincer, C. Acar, Int. J. Hydrogen Energy 40 (2015) 11094–11111. DOI: 10.1016/j.ijhydene.2014.12.035

[5]. J.D. Holladay, J. Hu, D.L. King, Y. Wang, Catal. Today 139 (2009) 244–260. DOI: 10.1016/j.cattod.2008.08.039

[6]. N.Z. Muradov, T.N. Veziroglu, Int. J. Hydrogen Energy 30 (2005) 225–237. DOI: 10.1016/j.ijhydene.2004.03.033

[7]. I. Dincer, Int. J. Hydrogen Energy 37 (2012) 1954–1971. DOI: 10.1016/j.ijhydene.2011.03.173

[8]. L. García, Compendium of Hydrogen Energy 83 (2015) 83–107. DOI: 10.1016/B978-1-78242-361-4.00004-2

[9]. Y. Kalinci, A. Hepbasli, I. Dincer, Int. J. Hydrogen Energy 34 (2009) 8799–8817. DOI: 10.1016/j.ijhydene.2009.08.078

[10]. L. Protasova, F. Snijkers, Fuel 181 (2016) 75–93. DOI: 10.1016/j.fuel.2016.04.110

[11]. J.O'M. Bockris, Int. J. Hydrogen Energy 38 (2013) 2579–2588. DOI: 10.1016/j.ijhydene.2012.12.026

[12]. M. Ball, M. Wietschel, Int. J. Hydrogen Energy 34 (2009) 615–627. DOI: 10.1016/j.ijhydene.2008.11.014

[13]. M. Balat, Int. J. Hydrogen Energy 33 (2008) 4013–4029. DOI: 10.1016/j.ijhydene.2008.05.047

[14]. J.D. Holladay, Y. Wang, J. Power Sources 282 (2015) 602–621. DOI: 10.1016/j.jpowsour.2015.01.079

[15]. Report of the Hydrogen Production Expert Panel: A Subcommittee of the Hydrogen & Fuel Cell Technical Advisory Committee, United States Department of Energy Washington, DC 20585 May 2013.

[16]. R. Horn, R. Schlogl, Catal. Lett. 145 (2015) 23–39. DOI: 10.1007/s10562-014-1417-z

[17]. K. Aasberg-Petersen, I. Dybkjær, C.V. Ovesen, N.C. Schjødt, J. Sehested, S.G. Thomsen, J. Nat. Gas Sci. Eng. 3 (2011) 423–459. DOI: 10.1016/j.jngse.2011.03.004

[18]. S.D. Angeli, G. Monteleone, A. Giaconia, A.A. Lemonidou, Int. J. Hydrogen Energy 39 (2014) 1979–1997. DOI: 10.1016/j.ijhydene.2013.12.001

[19]. T.L. LeValley, A.R. Richard, M. Fan, Int. J. Hydrogen Energy 39 (2014) 16983–17000. DOI: 10.1016/j.ijhydene.2014.08.041

[20]. U. Izquierdo, V.L. Barrio, J.F. Cambra, J. Requies, M.B. Guemez, P.L. Arias, G. Kolb, R. Zapf, A.M. Gutierrez, J.R. Arraibi, Int. J. Hydrogen Energy 37 (2012) 7026–7033. DOI: 10.1016/j.ijhydene.2011.11.048

[21]. V.D. Santoa, A. Gallo, A. Naldoni, M. Guidotti, R. Psaro, Catal. Today 197 (2012) 190–205. DOI: 10.1016/j.cattod.2012.07.037

[22]. S. Damyanova, B. Pawelec, K. Arishtirova, J.L.G. Fierro, Int. J. Hydrogen Energy 37 (2012) 15966–15975. DOI: 10.1016/j.ijhydene.2012.08.056

[23]. D.A.J.M. Ligthart, J.A.Z. Pieterse, E.J.M. Hensen, Appl. Catal. A 405 (2011) 108–119. DOI: 10.1016/j.apcata.2011.07.035

[24]. G. Nahar, V. Dupont, Rec. Patents Chem. Eng. 6 (2013). 8–42. DOI: 10.2174/2211334711306010003

[25]. C.H. Bartholomew, Appl. Catal. A 2012 (2001) 17–60. DOI: 10.1016/S0926-860X(00)00843-7

[26]. J.A. Moulijn, A.E. Diepen, F. Kapteijn, Appl. Catal. A 212 (2001) 3–16. DOI: 10.1016/S0926-860X(00)00842-5

[27]. K.O. Christensen, D. Chen, R. Lødeng, A. Holmen, Appl. Catal. A 314 (2006) 9–22. DOI: 10.1016/j.apcata.2006.07.028

[28]. J. Zhu, X. Peng, L. Yao, J. Shen, D. Tong, C. Hu, Int. J. Hydrogen Energy 36 (2011) 7094–7104. DOI: 10.1016/j.ijhydene.2011.02.133

[29]. I.Z. Ismagilov, E.V. Matus, D.V. Nefedova, V.V. Kuznetsov, S.A. Yashnik, M.A. Kerzhentsev, Z.R. Ismagilov, Kinet. Catal. 56 (2015) 394–402. DOI: 10.1134/S0023158415030064

[30]. S. Li, J. Gong, Chem. Soc. Rev. 43 (2014) 7245–7256. DOI: 10.1039/C4CS00223G

[31]. K. Fang, J. Ren, Y. Sun, J. Mol. Catal. A 229 (2005) 51–58. DOI: 10.1016/j.molcata.2004.10.055

[32]. S. He, H. Wu, W. Yu, L. Mo, H. Lou, H. Zheng, Int. J. Hydrogen Energy 34 (2008) 839–843. DOI: 10.1016/j.ijhydene.2008.10.072

[33]. S. He, X. Zheng, L. Mo, W. Yu, H. Wanga, Y. Luo, Mater. Res. Bull. 49 (2014) 108–113. DOI: 10.1016/j.materresbull.2013.08.051

[34]. D. Baudouin, U. Rodemerck, F. Krumeich, A. Mallmann, R.C. Szeto, H. Ménard, L. Veyre, J.-P. Candy, P.B. Webb, C. Thieuleux, C. Copéret, J. Catal. 297 (2013) 27–34. DOI: 10.1016/j.jcat.2012.09.011

[35]. J. Juan-Juan, M.C. Roman-Martınez, M.J. Illan-Gomez, Appl. Catal. A 355 (2009) 27–32. DOI: 10.1016/j.apcata.2008.10.058

[36]. J.M. García-Vargas, J.L. Valverde, A. Lucas-

Consuegra, B. Gómez-Monedero, P. Sánchez, F. Dorado, Appl. Catal. A 431-432 (2012) 49–56. DOI: 10.1016/j.apcata.2012.04.016
[37]. D. Liu, Y. Wang, D. Shi, X. Jia, X. Wang, A. Borgna, R. Lau, Y. Yang, Int. J. Hydrogen Energy 37 (2012) 10135–10144. DOI: 10.1016/j.ijhydene.2012.03.158
[38]. S. Somacescu, M. Florea, P. Osiceanu, J.M. Calderon-Moreno, C. Ghica, J.M. Serra, J. Nanopart. Res. 17 (2015) 426. DOI: 10.1007/s11051-015-3206-z
[39]. Z. Hou, O. Yokota, T. Tanaka, T. Yashima, Appl. Surf. Sci. 233 (2004) 58–68. DOI: 10.1016/j.apsusc.2004.03.223
[40]. I.Z. Ismagilov, E.V. Matus, V.V. Kuznetsov, M.A. Kerzhentsev, S.A. Yashnik, I.P. Prosvirin, N. Mota, R.M. Navarro, J.L.G. Fierro, Z.R. Ismagilov, Int. J. Hydrogen Energy 39 (2014) 20992–21006. DOI: 10.1016/j.ijhydene.2014.10.044
[41]. Y. Wang, L. Wang, N. Gan, Z.Y. Lim, C. Wu, J. Peng, W.G. Wang, Int. J. Hydrogen Energy 39 (2014) 10971–10979. DOI: 10.1016/j.ijhydene.2014.05.074
[42]. A.J. Abreu, A.F. Lucrédio, E.M. Assaf, Fuel. Process. Technol. 102 (2012) 140–145. DOI: 10.1016/j.fuproc.2012.04.030
[43]. D. Li, Y. Nakagawa, K. Tomishige, Appl. Catal. A 408 (2011) 1–24. DOI: 10.1016/j.apcata.2011.09.018
[44]. I.Z. Ismagilov, E.V. Matus, V.V. Kuznetsov, N. Mota, R.M. Navarro, Kerzhentsev, Z.R. Ismagilov, J.L.G. Fierro, Catal. Today 210 (2013) 10–18. DOI: 10.1016/j.cattod.2012.12.007
[45]. S. Gopalakrishnana, M.G. Faga, I. Miletto, S. Coluccia, G. Caputo, S. Sau, A. Giaconia, G. Berlier, Appl. Catal. B 138-139 (2013) 353–361. DOI: 10.1016/j.apcatb.2013.02.036
[46]. A.J. Majewski, J. Wood, W. Bujalski, Int. J. Hydrogen Energy 38 (2013) 14531–14541. DOI: 10.1016/j.ijhydene.2013.09.017
[47]. V.M. Gonzalez-Delacruz, J.P. Holgado, R. Pereñíguez, A. Caballero, J. Catal. 257 (2008) 307–314. DOI: 10.1016/j.jcat.2008.05.009
[48]. V.M. Gonzalez-Delacruz, F. Ternero, R. Pereñíguez, A. Caballero, J.P. Holgado, Appl. Catal. A 384 (2010) 1–9. DOI: 10.1016/j.apcata.2010.05.027
[49]. I.Z. Ismagilov, E.V. Matus, V.V. Kuznetsov, N. Mota, R.M. Navarro, S.A. Yashnik, I.P. Prosvirin, M.A. Kerzhentsev, Z.R. Ismagilov, J.L.G. Fierro, Appl. Catal. A 481 (2014) 104–115. DOI: 10.1016/j.apcata.2014.04.042
[50]. M.A. Naeem, A.S. Al-Fatesh, A.H. Fakeeha, A.E. Abasaeed, Int. J. Hydrogen Energy 39 (2014) 17009–17023. DOI: 10.1016/j.ijhydene.2014.08.090
[51]. L. Zhang, X. Wang, B. Tan, U.S. Ozkan, J. Mol. Catal. A 297 (2009) 26–34. DOI: 10.1016/j.molcata.2008.09.011
[52]. H. Li, H. Xu, J. Wang, J. Natural. Gas Chem. 20 (2011) 1–8. DOI: 10.1016/S1003-9953(10)60156-9
[53]. K. Urasaki, Y. Tanpo, Y. Nagashima, R. Kikuchi, S. Satokawa, Appl. Catal. A 452 (2013) 174–178. DOI: 10.1016/j.apcata.2012.06.021
[54]. W. Yang, D. He, Appl. Catal. A 524 (2016) 94–104. DOI: 10.1016/j.apcata.2016.06.026
[55]. F. Liu, L. Zhao, H. Wang, X. Bai, Y. Liu, Int. J. Hydrogen Energy 39 (2014) 10454–10466. DOI: 10.1016/j.ijhydene.2014.05.036
[56]. F. Bentaleb, M. Che, A.-C. Dubreuil, C. Thomazeau, E. Marceau, Catal. Today 235 (2014) 250–255. DOI: 10.1016/j.cattod.2014.02.020
[57]. R. Murugavel, P. Davis, V. Shete, Inorg. Chem. 42 (2003) 4696–4706. DOI: 10.1021/ic034317m
[58]. K. Wada, T. Mitsudo, Catal. Surv. Asia 9 (2005) 229–241. DOI: 10.1007/s10563-005-9158-z
[59]. A.J. Ward, A.F. Masters, T. Maschmeyer, Chapter 3 Metallasilsesquioxanes: Molecular Analogues of Heterogeneous Catalysts, 2011. P. 135–166, In: C. Hartmann-Thompson (ed.), *Applications of Polyhedral Oligomeric Silsesquioxanes*, Advances in Silicon Science 3, Springer Science + Business Media B.V. DOI: 10.1007/978-90-481-3787-9_3
[60]. N. Maxim, H.C.L. Abbenhuis, P.J. Stobbelaar, B.L. Mojet, R.A. van Santen, Phys. Chem. Chem. Phys. 1 (1999) 4473–4477. DOI: 10.1039/A903684I
[61]. N. Maxim, P.M.C. Magusin, P.J. Kooyman, J.H.M.C. van Wolput, R.A. van Santen, H.C.L. Abbenhuis, Chem. Mater. 13 (2001) 2958–2964. DOI: 10.1021/cm010272g
[62]. N. Maxim, Metal silesquioxanes as precursors to microporous metallosilicates. PhD Thesis, Eindhoven: Technische Universiteit Eindhoven, 2002. ISBN 90-386-2683-5
[63]. H. Kaneko, S. Taku, Y. Tamaura, Solar Energy 85 (2011) 2321–2330. DOI: 10.1016/j.solener.2011.06.019
[64]. A. Fina, D. Tabuani, F. Carniato, A. Frache, E. Boccaleri, G. Camino, Thermochim. Acta 440 (2006) 36–42. DOI: 10.1016/j.tca.2005.10.006
[65]. M.F.P. Silva, J.R. Matos, P.C. Isolani, J. Therm. Anal. Calorim. 94 (2008) 305–311. DOI: 10.1007/s10973-007-8906-x
[66]. A. Małecki, R. Gajerski, S. Łabuś, B. Prochowska-Klisch, K.T. Wojciechowski, J. Therm. Anal. Calorim. 60 (2000) 17–23. DOI: 10.1023/A:1010155931266
[67]. E. Mikuli, A. Migdał-Mikuli, R. Chyży, B. Grad, R. Dziembaj, Thermochim. Acta 370 (2001) 65–71. DOI: 10.1016/S0040-6031(00)00770-X

[68]. B. Jankovic, S. Mentus, D. Jelić, Physica B 404 (2010) 2263–2269. DOI: 10.1016/j.physb.2009.04.024
[69]. F. Pompeo, N.N. Nichio, M.G. Gonzalez, M. Montes, Catal. Today 107-108 (2005) 856–862. DOI: 10.1016/j.cattod.2005.07.024
[70]. G.P. Androutsopoulos, C.E. Salmas, Ind. Eng. Chem. Res. 39 (2000) 3747–3763. DOI: 10.1021/ie0001624
[71]. T.D. Nguyen-Phan, M.B. Song, E.J. Kim, E.W. Shin, Micropor. Mesopor. Mater. 119 (2009) 290–298. DOI: 10.1016/j.micromeso.2008.10.039
[72]. J. Gao, J. Guo, D. Liang, Z. Hou, J. Fei, X. Zheng, Int. J. Hydrogen Energy 33 (2008) 5493–5500. DOI: 10.1016/j.ijhydene.2008.07.040
[73]. X. Chen, A.R. Tadd, J.W. Schwank, J. Catal. 251 (2007) 374–387. DOI: 10.1016/j.jcat.2007.07.031
[74]. B. Li, X. Xu, S. Zhang, Int. J. Hydrogen Energy 38 (2013) 890–900. DOI: 10.1016/j.ijhydene.2012.10.103
[75]. R.V. Wandekar, M. Ali (Basu), B.N. Wani, S.R. Bharadwaj, Mater. Chem. Phys. 99 (2006) 289–294. DOI: 10.1016/j.matchemphys.2005.10.025
[76]. B. Scheffer, P. Molhoek, J.A. Moulijn, Appl. Catal. 46 (1989) 11–30. DOI: 10.1016/S0166-9834(00)81391-3
[77]. H. Mori, C. Wen, J. Otomo, K. Eguchi, H. Takahashi, Appl. Catal. A 245 (2003) 79–85. DOI: 10.1016/S0926-860X(02)00634-8
[78]. J.S. Lisboa, L.E. Terra, P.R.J. Silva, H. Saitovitch, F.B. Passos, Fuel Process. Technol. 92 (2011) 2075–2082. DOI: 10.1016/j.fuproc.2011.06.011
[79]. S. Pengpanich, V. Meeyoo, T. Rirksomboon, Catal. Today 93-95 (2004) 95–105. DOI: 10.1016/j.cattod.2004.06.079
[80]. J.A. Montoya, E. Romero-Pascual, C. Gimon, P. Del Angel, A. Monzón, Catal. Today 63 (2000) 71–85. DOI: 10.1016/S0920-5861(00)00447-8
[81]. T. Takeguchi, S.N. Furukawa, M. Inoue, J. Catal. 202 (2001) 14–24. DOI: 10.1006/jcat.2001.3249
[82]. J.C. Escritori, S.C. Dantas, R.R. Soares, C.E. Hori, Catal. Commun. 10 (2009) 1090–1094. DOI: 10.1016/j.catcom.2009.01.001
[83]. T. Takeguchi, S.N. Furukawa, M. Inoue, K. Eguchi, Appl. Catal. A 240 (2003) 223–233. DOI: 10.1016/S0926-860X(02)00449-0
[84]. Q. Jing, L. Fang, H. Lou, X. Zheng, J. Rare Earths 27 (2009) 431–436. DOI: 10.1016/S1002-0721(08)60265-3